Geochemistry, Geophysics, Geosystems

RESEARCH ARTICLE
10.1029/2021GC009750

A Pulse of Meteoric Subsurface Fluid Discharging Into the Chukchi Sea During the Early Holocene Thermal Maximum (EHTM)

Ji-Hoon Kim[1], Wei-Li Hong[2], Marta E. Torres[3], Jong-Sik Ryu[4], Moo-Hee Kang[1], Dukki Han[5], Seung-Il Nam[6], Jin Hur[7], Dong-Chan Koh[8], Frank Niessen[9], Dong-Hun Lee[10,11], Kwangchul Jang[6], James William Buchanan Rae[12], and Meilian Chen[13]

[1]Petroleum & Marine Division, Korea Institute of Geoscience and Mineral Resources, Daejeon, South Korea, [2]Department of Geological Sciences, Stockholm University, Stockholm, Sweden, [3]College of Earth, Ocean, and Atmospheric Sciences, Oregon State University, Corvallis, OR, USA, [4]Department of Earth and Environmental Sciences, Pukyong National University, Busan, South Korea, [5]Department of Marine Molecular Bioscience, Gangneung-Wonju National University, Gangneung-si, Gangwon-do, South Korea, [6]Division of Glacial Environment Research, Korea Polar Research Institute, Incheon, South Korea, [7]Department of Environment & Energy, Sejong University, Seoul, South Korea, [8]Geologic Environment Division, Korea Institute of Geoscience and Mineral Resources, Daejeon, South Korea, [9]Alfred Wegener Institute, Helmholtz Centre for Polar and Marine Research (AWI), Bremerhaven, Germany, [10]Department of Marine Sciences and Convergent Technology, Hanyang University ERICA Campus, Ansan, South Korea, [11]Marine Environment Research Division, National Institute of Fisheries Science, Busan, South Korea, [12]School of Earth & Environmental Sciences, University of St Andrews, St Andrews, UK, [13]Environmental Program, Guangdong Technion-Israel Institute of Technology, Shantou, China

Abstract The response of Arctic Ocean biogeochemistry to subsurface flow driven by permafrost thaw is poorly understood. We present dissolved chloride and water isotopic data from the Chukchi Sea Shelf sediments that reveal the presence of a meteoric subsurface flow enriched in cations with a radiogenic Sr fingerprint. This subsurface fluid is also enriched in dissolved inorganic carbon and methane that bear isotopic compositions indicative of a carbon reservoir modified by reactions in a closed system. Such fluid characteristics are in stark contrast with those from other sites in the Chukchi Sea where the pore water composition shows no sign of meteoric input, but reflect typical biogeochemical reactions associated with early diagenetic sequences in marine sediment. The most likely source of the observed subsurface flow at the Chukchi Sea Shelf is from the degradation of permafrost that had extended to the shelf region during the Last Glacial Maximum. Our data suggest that the permafrost-driven subsurface flow most likely took place during the 2–3°C warming in the Early Holocene Thermal Maximum. This time scale is supported by numerical simulation of pore water profiles, which indicate that a minimum of several thousand years must have passed since the cessation of the subsurface methane-bearing fluid flow.

Plain Language Summary The permafrost in the Arctic Ocean has repeatedly formed and thawed with global climate change through geological time with significant consequences for the marine subsurface environment. In addition to biogeochemical reactions in the sediment, global climate impacts the regional water and carbon cycles. Here we address the potential influence of permafrost dynamics on the geochemical cycles in the Chukchi Sea sediments. Pore water composition at the Chukchi Sea Shelf shows a freshwater signature indicative of a meteoric contribution. The characteristics of both pore water and gas in the shelf site were remarkably different from those observed in other areas of the Chukchi Sea. To understand why and when these unique properties developed, we simulated the pore water and gas data with a numerical model. We found that the observed freshwater signature and unique composition at the Chukchi Sea Shelf were likely caused by a paleo-subsurface flow associated with natural permafrost thaw during the Early Holocene, when the Arctic region was at least 2–3°C warmer than today. Though the results of our study are significant, more research is needed to understand and predict the change in the marine subsurface environment as permafrost thaws in response to rapid global warming.

Ji-Hoon Kim, Wei-Li Hong, and Marta E. Torres equally contributed to this work as co-first authors.

Key Points:

- Pore water chemistry from the Chukchi Sea Shelf reveals meteoric subsurface flow in response to permafrost thaw at the Early Holocene Thermal Maximum
- Concentration and isotope data from carbon pools point to a migrating fluid input from an old carbon reservoir
- Subsurface flow is important for the budget of carbon and other elements related to permafrost thaw

Supporting Information:

Supporting Information may be found in the online version of this article.

Correspondence to:

J.-H. Kim,
save@kigam.re.kr

Citation:

Kim, J.-H., Hong, W.-L., Torres, M. E., Ryu, J.-S., Kang, M.-H., Han, D., et al. (2021). A pulse of meteoric subsurface fluid discharging into the Chukchi Sea during the Early Holocene Thermal Maximum (EHTM). *Geochemistry, Geophysics, Geosystems*, *22*, e2021GC009750. https://doi.org/10.1029/2021GC009750

Received 26 FEB 2021
Accepted 13 JUL 2021

1. Introduction

The Arctic region has experienced repeated permafrost formation and degradation through geological time. Warm periods lead to permafrost thaw, which directly influences hydrology and ecosystem functioning (Christensen et al., 2004; Smith et al., 2005). Hydrological models forecast an enhancement of subsurface flow from permafrost degradation (Bense et al., 2009), consistent with recent predictions of an increase in groundwater flow by landscape evolution and permafrost degradation as the planet warms (Young et al., 2020). There are considerable efforts to understand the consequences of the anticipated subsurface flow in the Arctic Ocean on biogeochemical cycling and mass inventories. For example, the enhanced discharge and migration of fluids modified by reactions in the subsurface significantly affect primary production and can lead to the release of methane (CH_4) to the atmosphere (Lapham et al., 2017; Sparrow et al., 2018). A CH_4 release in response to a decrease cryosphere extent will have a positive feedback on global warming due to the high radiative potential of this greenhouse gas (Schuur et al., 2015). Because of the importance of understanding this feedback loop on Earth's climate, efforts have been made to monitor CH_4 fluxes from Arctic lakes and wetlands (Garcia-Tigreros Kodovska et al., 2016) and to estimate the CH_4 input to the ocean via water column investigations (Lapham et al., 2017; Lecher et al., 2016; Sparrow et al., 2018).

Here we present chemical and isotopic data of pore water and dissolved gas samples from four sediment cores retrieved from the Chukchi Sea Shelf to the basin proper (Figure 1). The freshwater discharge inferred from dissolved chloride concentration and water isotopic data provides a basis to evaluate how subsurface flow impacts elemental budgets and carbon cycling in the Chukchi Sea Shelf. The pore water data indicate that discharging fluid may have supplied the coastal ocean with CH_4, alkalinity, silica, barium, and boron enriched in ^{10}B, as well as radiogenic strontium (^{87}Sr). The fluid delivers ^{13}C-enriched dissolved inorganic carbon (DIC) to the shelf from a carbon reservoir modified by reactions in a closed system. Based on paleoceanographic reconstructions (Stein et al., 2017) and our numerical simulation, we postulate that the anomalous pore water data from the Chukchi Sea Shelf likely reflect a hydrological response to 2–3°C warming in the middle and high latitudes of the northern hemisphere during the Early Holocene Thermal Maximum (EHTM) (Renssen et al., 2009). Collectively, our results are indicative of potential changes in fluid elemental and isotopic compositions associated with subsurface flow by permafrost thaw. To date, there are only a handful of studies that systematically investigate the interactions between the cryo- and hydrospheres in the Arctic Ocean (e.g., Hong et al., 2019; Sparrow et al., 2018), and none that can be used to document changes due to past perturbations of these Earth system components. Our inferences that a paleo-subsurface flow resulted from global warming in the past may serve as an analog to the expected environmental changes as our planet warms in the future.

2. Regional Setting

We present data from four sediment cores recovered from the Chukchi Sea by Jumbo Piston Corer (JPC) during the ARA06C Expedition in 2015 and complement our findings with records from a previously recovered core in the region (core ARA2B-1A) (Stein et al., 2017). We also compare data from other cores from the Beaufort Sea regions (Figure 1), where specific aspects of pore water geochemistry, but not all, were investigated.

The Chukchi Sea extends from 66°N in the south to the edge of the Arctic Basin in the north, covering an area of 620,000 km^2 (Jakobsson, 2002), and has a broad and shallow continental shelf. The Chukchi Borderland is an adjacent fragment of continental crust extending north into the Canada Basin of the Arctic Ocean (Dove et al., 2014). The Beaufort Shelf, located in the eastern part of the Chukchi Sea, is up to ~150 km wide with an average bathymetric gradient of 1 m/km (Gwiazda et al., 2018) (Figure 1).

The Chukchi Sea has been influenced by Laurentide Ice Sheet dynamics over the last 71 kyr (extending to Marine Isotope Stage [MIS] 4) (Dove et al., 2014). Ice sheet plow marks are commonly observed in the Chukchi Sea at water depths ranging from ~130 to ~350 m. They are attributed to ice-shelf disintegration during the last deglaciation (Polyak et al., 2007). Glaciogenic landforms (lineations, morainic ridges), curvilinear to sinuous symmetric/asymmetric ridges in the shelf edge, till wedges, and debris lobes have also been documented, indicative of glacier influence (Jakobsson et al., 2014).

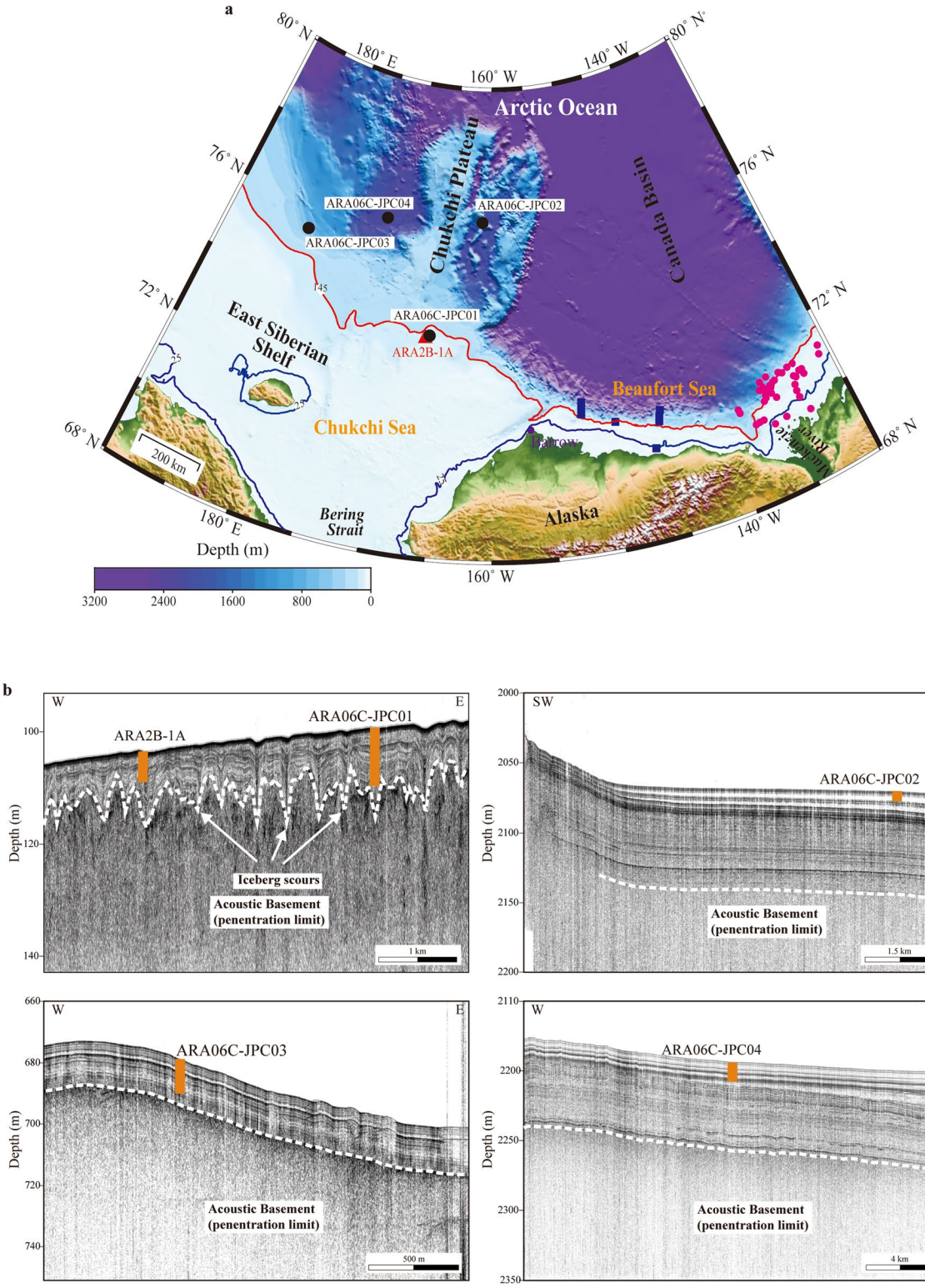

Figure 1. (a) Major physiographic features of the Chukchi Sea and the location of sites (black closed circles) investigated during the *IBRV* ARAON ARA06C Expedition. The solid red line (water depth: 145 m) is the expected front line of permafrost during the Last Glacial Maximum when the sea level was 120 m below the present. The solid blue line (water depth: 25 m) is the predicted extent of permafrost at present time, based on the seismic velocity extrapolations from the Beaufort Sea coverage permafrost (>2,000 m/s) (Brothers et al., 2016). Red closed triangle: ARA2B-1A of Stein et al. (2017), blue closed squares: sites in the Alaskan Beaufort Sea Shelf and Slope of Coffin et al. (2013) and Lorenson et al. (2016), magenta closed circles: Canadian Beaufort Sea sites of Gwiazda et al. (2018). (b) Chirp sub-bottom profiles from Sites ARA06C-JPC01, ARA06C-JPC02, ARA06C-JPC03, and ARA06C-JPC04, collected during this study.

Table 1
Summaries of Location, Water Depth, and Depth of the SMT in Each Site From the ARA06C Expedition

Site	Latitude	Longitude	Water depth (m)	Total sediment length (m)	Depth of the SMT (mbsf)
ARA06C-JPC01	73° 37.2217′ N	166° 25.7329′ W	100	10.4	~4.5
ARA06C-JPC02	76° 36.1612′ N	161° 10.0811′ W	2,077	7.4	–
ARA06C-JPC03	75° 32.0053′ N	178° 44.0631′ E	715	11.3	–
ARA06C-JPC04	76° 25.8640 N	172° 40.6021′ W	2,240	13.9	–

Note. "–" denotes not reach.
Abbreviation: SMT, sulfate-methane transition.

Whereas erosional events by Laurentide-sourced ice to the Chukchi Sea during MIS 4 have been reported (Polyak et al., 2007), the scenario during the Last Glacial Maximum (LGM; 26.5–19.0 ka BP) is still being debated. Glaciogenic landforms in the Chukchi Borderland have been proposed as evidence for the absence of large ice sheets in the Late Pleistocene, although the presence of a local Chukchi ice rise cannot be ruled out (Polyak et al., 2007). In contrast, glaciogenic landforms attributed to a large (~1 km-thick) ice sheets spreading into the working area from the East Siberian Sea are interpreted to be older than the most recent glacial period (Niessen et al., 2013), consistent with inferences for the northwestern progression of the Laurentide Ice Sheet during the last glaciation based on ice-scouring records in the Beaufort Shelf (Brothers et al., 2016).

Based on comparisons with the adjacent Beaufort Continental Shelf, permafrost in the Chukchi Sea at the LGM may have extended to the shelf area equivalent to present water depths of <145 m (Brothers et al., 2016). This corresponds to the region where our core ARA06C-JPC01 was recovered from (Figure 1; Table 1), but we note that the permafrost extent in the Chukchi Sea cannot be fully ascertained due to the limited seismic and core data available. Presently, subsea ice-bearing permafrost in the Beaufort Shelf occurs in water depths <25 m, as reflected by high velocity returns in the seismic data (Brothers et al., 2016).

3. Materials and Methods

3.1. Site Description

The study cores were retrieved from the Chukchi Sea Shelf (ARA06C-JPC01), the Northwind Basin (ARA06C-JPC02), the East Siberia Continental Slope (ARA06C-JPC03), and the Chukchi Basin (ARA06C-JPC04). Site locations and water depths are listed in Table 1 and plotted in Figure 1.

Based on the bathymetry and chirp seismic data, the seafloor at the location of Site ARA06C-JPC01 and the nearby Site ARA2B-1A (Stein et al., 2017) shows abundant ice-scouring infilled with well-stratified Holocene sediment (Figure 1b). Biomarker data from Site ARA2B-1A revealed that the millennial variability of sea ice in the Chukchi Sea has been modulated by changes in surface water delivery from the Pacific Ocean as well as by solar insolation during the Holocene (Stein et al., 2017). The sediment section at Site ARA06C-JPC02 shows three seismic acoustic units: a sub-continuous to discontinuous layer overlaid by a stratified layer with a uniform thickness of ~40 m, and a well-layered and transparent sediment section of fine-grained homogeneous pelagic sediment. At Site ARA06C-JPC03, the seismic data display an acoustically continuous and well-stratified sediment section with a uniform thickness of ~20 m, which drapes the chaotic unstratified glacial till. Continuous to sub-continuous reflectors at Site ARA06C-JPC04 overlie the chaotic acoustic basement, a wavy to semi-transparent sediment layer, and a well-stratified to transparent sediment section interpreted as fine-grained pelagic sediment (Figure 1b).

We compare our data with those from the Beaufort Sea regions where the pore water composition was not fully characterized. The reported data from the Alaskan Beaufort Sea include concentrations and isotopic compositions of the carbon reservoirs and the metabolites associated with carbon cycling, but lack information on chloride or water isotopic compositions (Coffin et al., 2013). The data set of the Canadian Beaufort Sea focuses on the freshening but does not include information on carbon metabolic pathways. Neither data

set includes other cations or the isotopic compositions of strontium and boron (Gwiazda et al., 2018; Paull et al., 2015), which provide information on sources and pathways of subsurface fluids.

3.2. Pore Water and Headspace Gas Sampling

Upon recovery, cores were immediately sectioned on deck at 1.4–3.0 m intervals. For headspace gas (HS) analyses, 3 ml sediment samples were taken with 5 ml cut-off plastic syringes from the freshly exposed end of each core section and extruded into 30 ml serum glass vials filled with 2 ml of saturated NaCl solution. The HS vials were capped with rubber septa and sealed with aluminum crimp caps.

We perforated holes in the core liner at 0.5–1.0 m intervals to extract pore water using Rhizons attached to acid-washed syringes. We were not able to collect pore water through the full retrieved core length of Site ARA06C-JPC01, because Rhizons could not penetrate the consolidated sediment below 7.84 mbsf (meters below seafloor). The extracted pore water was filtered through a 0.20 μm disposable polytetrafluoroethylene filter, before subsampling for onboard and post-cruise analyses. For the analyses of cations and $^{87}Sr/^{86}Sr$, pore water was collected in acid-washed high-density polyethylene (HDPE) bottles and acidified with ultra-pure concentrated HNO_3. Un-acidified subsamples for boron isotope analysis were collected in acid-washed HDPE bottles. Subsamples for stable isotopic properties of water ($\delta^{18}O_{H2O}$ and δD_{H2O}) and dissolved inorganic carbon ($\delta^{13}C_{DIC}$) were collected in 2 ml septum screw-lid glass vials. Samples for $\delta^{13}C_{DIC}$ analysis were preserved with $HgCl_2$. All pore water subsamples were refrigerated until analysis.

3.3. Pore Water and Headspace Gas Analyses

Chlorinity (Cl^-), alkalinity, and nutrients (NH_4^+ and PO_4^{3-}) were measured onboard during the ARA06C Expedition. Cl^- and alkalinity were determined immediately after pore water extraction by visual titration with 0.1 M $AgNO_3$ and 0.02 M HCl, respectively. The reproducibility of Cl^- and alkalinity by repeated analysis of IAPSO standard seawater was <2% and <0.5%, respectively. NH_4^+ and PO_4^{3-} were measured spectrophotometrically (UV-2450, Shimazu) at 640 and 885 nm, respectively. Sulfate (SO_4^{2-}) was analyzed by an ion chromatography (ICS-1500, Dionex) in the Korea Institute of Geoscience and Mineral Resources (KIGAM).

Major and minor cations (Na^+, K^+, Mg^{2+}, Ca^{2+}, Ba^{2+}, B, Sr^{2+}, and H_4SiO_4) were analyzed by an inductively coupled plasma-optical emission spectrometer (Optima 8300 ICP-OES, Perkin Elmer) in the Korea Basic Sciences Institute (KBSI). The reproducibility from repeated analyses of reference materials (SLRS-4 and NASS-5) was <5%.

$\delta^{18}O_{H2O}$ and δD_{H2O} were determined with a wavelength-scanned cavity ring-down spectroscopy (L2120-i, Picarro Inc.) in the KIGAM, with the reproducibility of 0.1‰ for $\delta^{18}O_{H2O}$ and 0.5‰ for δD_{H2O}. $\delta^{13}C_{DIC}$ was analyzed with a Finnigan DELTA-Plus mass spectrometer using a Gas-Bench II automated sampler at Oregon State University. The precision and accuracy are better than 0.15‰ and 0.07‰, based on the multiple standard measurements. Isotopic values are reported in the conventional δ-notation relative to V-SMOW for hydrogen and oxygen, and V-PDB for carbon.

Dissolved Sr^{2+} in pore water was separated for isotopic analysis using Sr-Spec columns (Eichrom). $^{87}Sr/^{86}Sr$ ratio was measured using a Neptune multi-collector inductively coupled plasma mass spectrometer (MC-ICP-MS, Thermo Scientific) in the KBSI. $^{87}Sr/^{86}Sr$ ratio was normalized to $^{86}Sr/^{88}Sr = 0.1194$, and repeated NBS 987 measurements yielded values of 0.71025 ± 0.00002 (2σ, $n = 24$).

Prior to boron isotope ($\delta^{11}B$) measurements, 10 μl of the pore water was purified using B-specific Amberlite IRA743 resin. The $\delta^{11}B$ signatures were analyzed with a Neptune MC-ICP-MS in the St. Andrews Isotope Geochemistry Laboratory. The analytical procedure was described in Rae et al. (2011), with long-term reproducibility of 0.2‰ (2σ) for samples of this type.

HS gas was extracted by heating the sediment samples in an oven at 60°C for 30 min and gas composition was measured by an Agilent 7890A gas chromatograph with flame ionization detector in the KIGAM. The reproducibility for hydrocarbon gas from repeated analysis of the mixtures standard gas was better than 4%.

Measured CH_4 concentration in the HS sample was converted to molar CH_4 concentration in the pore water by Equation 1 (Riedel et al., 2006).

$$CH_4 = \left(X_M \times P_{atm} \times V_H\right) / \left(R \times T \times \phi \times V_S\right) \quad (1)$$

where, V_H = volume of the sample vial headspace, V_S = volume of the sediment sample, X_M = molar fraction of CH_4 in the HS gas (obtained from GC analysis), P_{atm} = pressure in the HS vial (assumed 1 atm), R = the universal gas constant, T = temperature of the HS vial in Kelvin, and ϕ = sediment porosity.

The carbon isotopic ratios of CH_4 and carbon dioxide (CO_2) in HS samples were analyzed using a compound-specific isotope ratio-monitoring gas chromatograph/mass spectrometer at Isotech Laboratories Inc. The carbon isotopes are reported in the conventional δ-notation relative to V-PDB. The reproducibility of the analyses was 0.1‰.

3.4. Physical Property Analysis

During the ARA06C Expedition, physical properties were determined on whole cores at 1 cm intervals using a multi-sensor-core-logger (MSCL-S, Geotek Ltd.). These include volume-specific magnetic susceptibility (Bartington MS-2 loop sensor), wet bulk density (gamma ray attenuation), and p-wave velocity (500 kHz plate transducers). On Site ARA2B-1A, magnetic susceptibility (Bartington MS-2F sensor) and wet bulk density (gamma ray attenuation) were measured on split cores after the cruise using the same MSCL-S device. The strong fluctuations of wet bulk density in the upper two meters of this core are artifacts from core transport and/or storage (Figure S1).

3.5. TOC Analysis

The bulk sediments from Site ARA06C-JPC01 were sampled continuously with 30 cm intervals and freeze-dried for 24 h. Dried samples were ground and homogenized in an agate mortar. Aliquots of powdered samples were used for the geochemical analyses. Total organic carbon (TOC) in the samples was measured using a Rock-Eval 6 (Vinci Technologies) in the KIGAM, summing up the pyrolyzed carbon and residual carbon (Kim et al., 2020). IFP 16000 was used as a standard (TOC = 3.28 ± 0.14 wt.%), and the analytical reproducibility was better than 2%.

4. Results and Discussion

4.1. Pore Water Freshening

The Cl^- concentration in pore waters at Site ARA06C-JPC01 shows a general decrease with depth from 537 mM at 0.20 mbsf to 508 mM at 6.84 mbsf (Figure 2; Table S1). The observed stepwise decreasing trend, rather than a smooth curve, is caused by the analytical challenges due to slight variations in color change at the titration end-point, which resulted in an error range of <2%. Notwithstanding the analytical uncertainty, the Cl^- trend at Site ARA06C-JPC01 is in contrast with the Cl^- profiles in the other three cores, which display only slight fluctuations in Cl^- concentration with depth. Assuming a bottom seawater value of 540 mM (Table S1), the maximum degree of freshening ($[Cl^-_{seawater} - Cl^-_{pore\ water}]/Cl^-_{seawater} \times 100$) at Site ARA06C-JPC01 is 6%.

Processes that explain fluid freshening in marine sediments include gas hydrate dissociation, meteoric water input, and dehydration of clay minerals (Kastner et al., 1991; Kim, Torres, Hong, et al., 2013). The good correlation between $\delta^{18}O_{H2O}$ and δD_{H2O} in pore waters from Site ARA06C-JPC01, coincident with the local meteoric water line (http://www-naweb.iaea.org/napc/ih/HIS_resources_gnip.html), points to a meteoric source for the freshened fluid. Furthermore, Cl^- concentrations in pore waters from Site ARA06C-JPC01 show positive correlations with $\delta^{18}O_{H2O}$ and δD_{H2O} (Figure 3) that negate explanations tied to gas hydrate dissociation and dehydration reactions (e.g., illitization and opal diagenesis) as the freshening cause (Kastner et al., 1991; Kim, Torres, Hong, et al., 2013). Rather, projected values of the $\delta^{18}O_{H2O}$ and δD_{H2O} to a zero Cl^- concentration are −19.2‰ and −160.0‰ (Figure 3), which are consistent with the depleted isotopic composition in precipitation at high latitudes. As a reference, the $\delta^{18}O_{H2O}$ and δD_{H2O} values of modern precipitation in Inuvik, Canada, are −18.8‰ and −143.7‰ (Gwiazda et al., 2018). It is likely that the observed

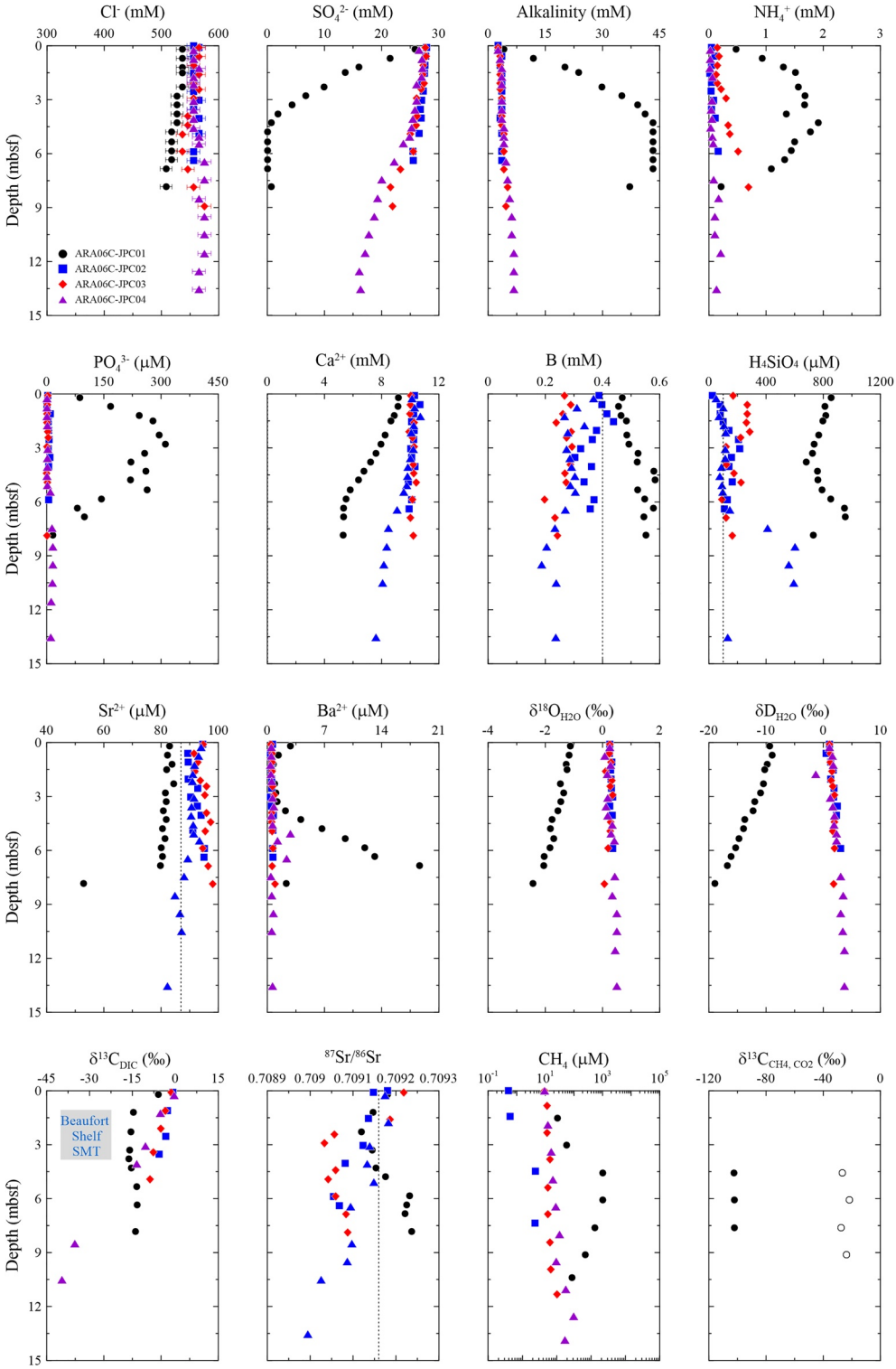

Figure 2. Data from Sites ARA06C-JPC01 (black closed circles), ARA06C-JPC02 (blue closed squares), ARA06C-JPC03 (red closed diamonds), and ARA06C-JPC04 (purple closed triangles) showing downcore profiles of Cl^{-}, SO_4^{2-}, alkalinity, NH_4^{+}, PO_4^{3-}, Ca^{2+}, B, H_4SiO_4, Sr^{2+}, and Ba^{2+} concentration; and isotopic ratios of water ($\delta^{18}O_{H2O}$ and δD_{H2O}), dissolved inorganic carbon ($\delta^{13}C_{DIC}$), and dissolved strontium ($^{87}Sr/^{86}Sr$) in pore waters. Also shown are the CH_4 and gas isotope results (closed symbols: $\delta^{13}C_{CH4}$, open symbols: $\delta^{13}C_{CO2}$) in headspace gases from Site ARA06C-JPC01. No headspace gas data are available from Sites ARA06C-JPC02, ARA06C-JPC03, and ARA06C-JPC04. The gray area in the downcore profile of $\delta^{13}C_{DIC}$ is the range of sulfate-methane transition (SMT) and $\delta^{13}C_{DIC}$ around the SMT in the Alaskan Beaufort Sea (Coffin et al., 2013). The black dashed lines in the pore water profiles show seawater values and error bars express only in Cl^{-} concentration of pore water (±2%).

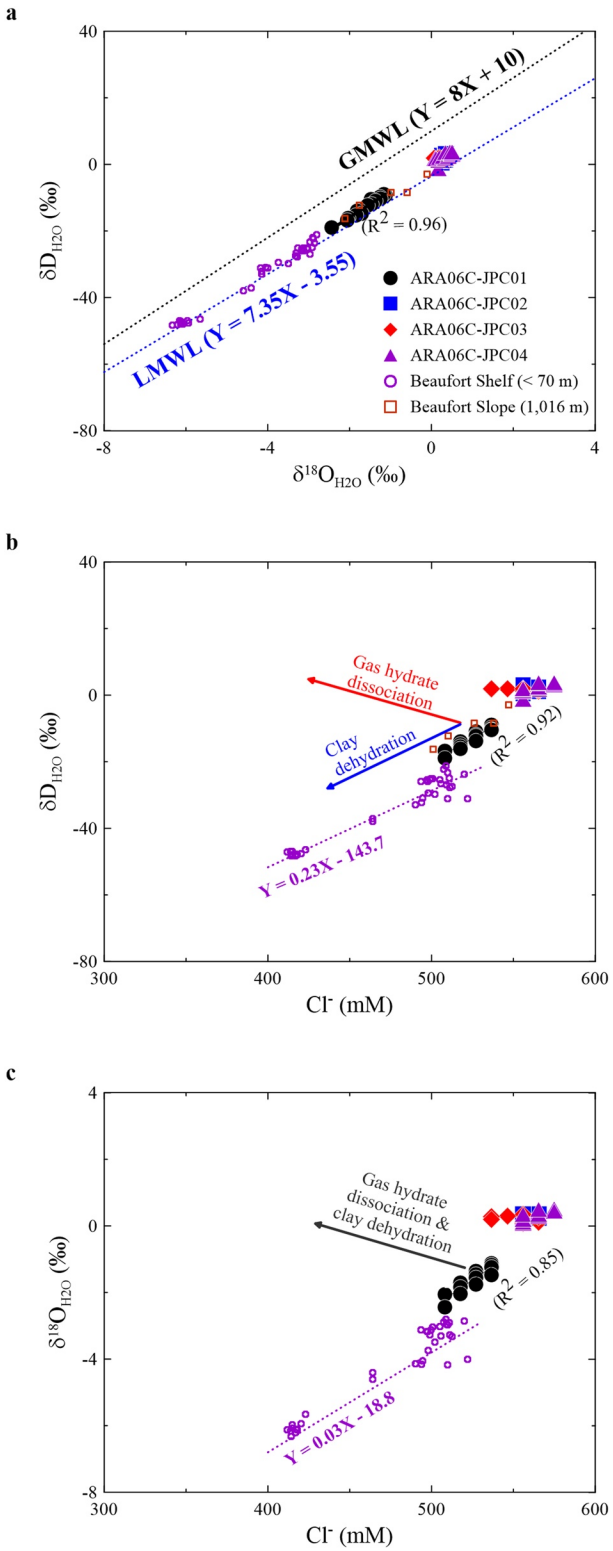

Figure 3. Scatter plots of (a) δD_{H2O} versus $\delta^{18}O_{H2O}$, (b) δD_{H2O} versus chlorinity (Cl^-), and (c) $\delta^{18}O_{H2O}$ versus Cl^- in pore waters from Sites ARA06C-JPC01 (black closed circles), ARA06C-JPC02 (blue closed squares), ARA06C-JPC03 (red closed diamonds), and ARA06C-JPC04 (purple closed triangles). Open symbols show data from the Canadian Beaufort Continental Shelf and Slope from Gwiazda et al. (2018), included for comparison. GMWL is global meteoric water line (Craig, 1961), and LMWL is local meteoric water line at Inuvik, Canada, by the Global Network of Isotopes in Precipitation (http://www-naweb.iaea.org/napc/ih/IHS_resources_gnip.html).

meteoric water was not sourced from modern precipitation but an ancient one; however, the corresponding data in the past, such as during full glacial conditions at the LGM, are more difficult to constrain. The average estimates presented by Fritz et al. (2011) have values of −33‰ and −258‰ for $\delta^{18}O_{H2O}$ and δD_{H2O}, respectively. Hence, the freshening at Site ARA06C-JPC01 can be predominantly attributed to a meteoric water source.

Pore waters from the sites cored farther offshore have relatively constant values of $\delta^{18}O_{H2O}$, δD_{H2O}, and Cl^- (Figure 3; Table S1), which are similar or slightly higher than those of present-day Atlantic waters (Pados et al., 2015). The pore water signals in these cores are thus attributed to the burial of Atlantic water without significant change in fluid source over the time corresponding to the cored depth.

The Cl^-, $\delta^{18}O_{H2O}$, and δD_{H2O} of pore waters from the Canadian Beaufort Sea show freshwater contributions from the shallow shelf to the slope with water depths greater than 1,000 m (Gwiazda et al., 2018; Paull et al., 2015) (Figures 1 and 3). This freshening has been attributed to: (a) downward infiltration of the Mackenzie River water to the shelf sediment, (b) relict submarine permafrost/gas hydrate decomposition input to the shelf edge, (c) submarine groundwater discharge to the slope, (d) freshwater extrusion in pingo-like features (PLFs), and (e) pre-Pleistocene waters from beneath the offshore permafrost. More recently, Gwiazda et al. (2018) showed that the freshening in pore water from the Beaufort Slope sediments is caused by regional groundwater flow and submarine groundwater that discharges as far as 150 km from the shore. Whether a similar set of mechanisms can explain the anomalous data observed at Site ARA06C-JPC01 is a matter of interest. As we discussed before, our isotopic data show that gas hydrate dissociation cannot be the cause for freshening at our site (Figure 3). Whereas the Holocene sediment supplied to the Beaufort Shelf is dominated by Mackenzie and Colville river systems (Coffin et al., 2013), an analogous connection to a riverine or nearby land source that can supply sediments or fluids to the location of Site ARA06C-JPC01 does not exist. Furthermore, available geophysical data show no PLFs or mounds in the region of Site ARA06C-JPC01 (Figure 1). Hence, the potential mechanism for the freshening at Site ARA06C-JPC01 is subsurface permafrost thaw or submarine groundwater discharge. These two sources are difficult to distinguish based on the geochemical data available because they are likely related as flow may be induced or enhanced by permafrost thaw. Therefore, in the following sections we use the term "subsurface flow" to discuss geochemical repercussions from a fluid supply associated with one or both of these freshening mechanisms.

4.2. Carbon Sources and Cycling

In the previous section we showed that the freshwater observed in the pore waters at Site ARA06C-JPC01 is clearly indicative of a meteoric subsurface fluid. We now investigate the associated changes to the carbon inventories at the Chukchi Sea Shelf sediment that are associated with the pulse of subsurface flow. Organic matter in anoxic marine sediment is primarily degraded by particular organic carbon sulfate reduction (POCSR) and methanogenesis (ME). Anaerobic oxidation of methane (AOM) by SO_4^{2-} occurs within the sulfate-methane transition (SMT), where SO_4^{2-} is depleted and CH_4 concentration starts to increase with depth. At Site ARA06C-JPC01, SO_4^{2-} is fully depleted at ∼4.5 mbsf, whereas the SMT depths are projected to be greater than 16 mbsf at the other sites (Figure 2; Table 1).

To constrain the rates of the various reactions involved, we constructed a numerical model to simulate the pore water profiles at Site ARA06C-JPC01 resulting from carbon cycling by applying a CrunchFlow code (Steefel et al., 2015) with a customized MATLAB routine that includes the four primary reactions: AOM, POCSR, ME, and authigenic carbonate precipitation. The transport-reaction model was developed by and detailed in Hong et al. (2016). We adopted the bottom seawater composition as the top boundary condition and assigned the lowermost values measured in the pore water composition as the lower boundary condition. We assigned an initial condition of a very shallow SMT (0.25 mbsf), which was derived from the same model when a high CH_4 concentration is assigned in the bottom cell (see Section 4.4 for justification of such initial condition). We first adjusted the kinetic constants for both POCSR and ME to match the observed NH_4^+ and PO_4^{3-} profiles by assigning C/N and C/P ratios of 10 and 100, respectively, and iteratively adjusted the assigned CH_4 supply at the lower boundary condition to match the observed SO_4^{2-} profile. Carbonate precipitation was constrained by matching the Ca^{2+} and Mg^{2+} profiles. We executed the model to reach a quasi-steady state condition. Whereas most of the profiles can be adequately modeled under the assumption of a steady state (Figure 4), the results indicate a significant excess in the measured DIC as compared to the

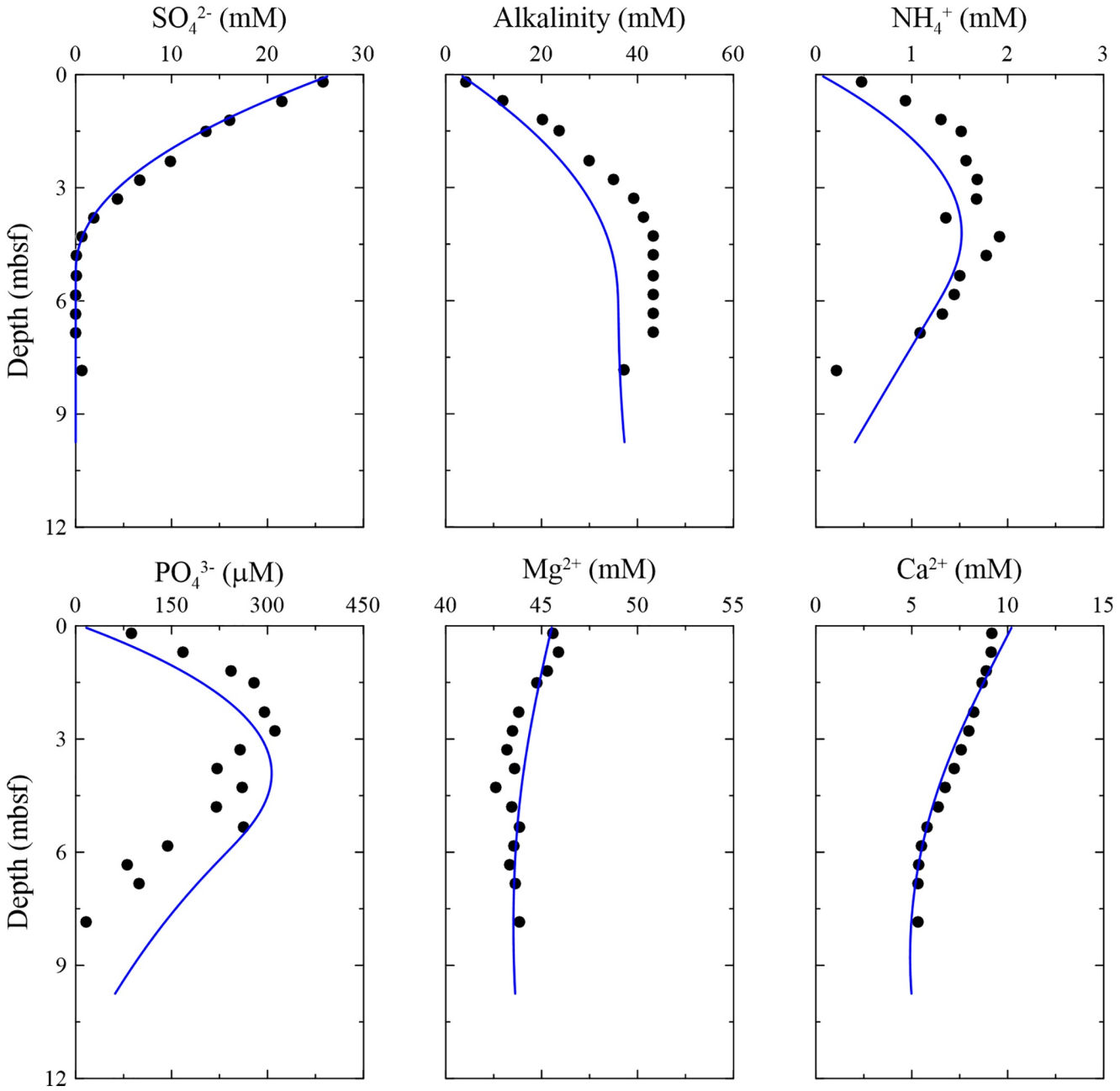

Figure 4. Downcore profiles of modeling results (blue solid line) in pore water from Site ARA06C-JPC01 by fitting the measured pore water profiles (black closed circles). *In situ* carbon cycling reactions included in the model are particular organic carbon sulfate reduction, methanogenesis, anaerobic oxidation of methane, and authigenic carbonate precipitation. The discrepant profiles of alkalinity between analyzed data and modeling results indicate the contribution of an allochthonous dissolved inorganic source.

level generated by *in situ* reactions in the model. A likely explanation for such a discrepancy includes an additional source of DIC other than those assigned in our numerical model.

AOM converts CH_4 to bicarbonate, resulting in the low $\delta^{13}C_{DIC}$ values (<−30‰) (e.g., Chatterjee et al., 2011) commonly observed at the SMT of continental margin sediments. However, the $\delta^{13}C_{DIC}$ values at the SMT of Site ARA06C-JPC01 are higher than such an expectation, reaching a minimum value of −16‰ (Figure 2; Table S1). These relatively high values for the $\delta^{13}C_{DIC}$ are distinct from those reported in the Alaskan Beaufort Sea, where the $\delta^{13}C_{DIC}$ ranges from −40 to −21‰ (Coffin et al., 2013) (Figure 2). The following sections aim at explaining the anomalous concentration and isotopic composition of the DIC at Site ARA06C-JPC01.

Our steady state assumption and the time scale of the pore water system evolution will be discussed in Section 4.4.

4.2.1. Dissolved Inorganic Carbon (DIC) Mass Balance

Assuming the major components of the DIC inventory to be: (a) DIC produced via POCSR (DIC_{POCSR}) and AOM (DIC_{AOM}); (b) DIC from a postulated old carbon pool (DIC_{OLD}); and (c) DIC consumption through carbonate precipitation (DIC_{CARB}); we can write a mass balance equation for the measured DIC concentration at the depth of SMT (DIC_{meas}, 43 mM) as:

$$\left[DIC_{meas}\right]=\left[DIC_{POCSR}\right]+\left[DIC_{AOM}\right]+\left[DIC_{OLD}\right]-\left[DIC_{CARB}\right] \quad (2)$$

We estimate $[DIC_{POCSR}]$ and $[DIC_{CARB}]$ from the concentrations of NH_4^+, Ca^{2+}, and Mg^{2+}. NH_4^+ concentration at the SMT is 1.8 mM higher than the bottom seawater value. Assuming a C/N molar ratio is 10 and all NH_4^+ is produced from POCSR, organic matter contributes 18 mM of DIC at the SMT. From the amount of DIC produced and the stoichiometric relationship (1:2) between SO_4^{2-} and DIC during POCSR, we can further estimate that 9 mM of SO_4^{2-} is consumed by organic matter, which leaves 20 mM of SO_4^{2-} consumed by AOM. The amount of DIC produced at the SMT through AOM is therefore 20 mM assuming a 1:1 stoichiometric ratio. Ca^{2+} and Mg^{2+} concentrations at the SMT are 3.0 and 6.8 mM lower than the concentrations in bottom seawater from Site ARA06C-JPC01, which means that there is 10 mM of DIC being precipitated as authigenic carbonates between sediment surface and the SMT. The only term left in Equation 2 is, therefore $[DIC_{OLD}]$, which can be estimated to be 15 mM.

4.2.2. Dissolved Inorganic Carbon (DIC) Isotopic Mass Balance

To unravel the fluid source that led to the unique $\delta^{13}C_{DIC}$ values in Site ARA06C-JPC01, we considered a carbon isotopic mass balance to account for the various potential contributions to the DIC reservoir, such that:

$$\delta^{13}C_{meas\text{-}DIC} = f_{AMO}\cdot\delta^{13}C_{AOM\text{-}DIC} + f_{POCSR}\cdot\delta^{13}C_{POCSR\text{-}DIC} + f_{OLD}\cdot\delta^{13}C_{OLD\text{-}DIC} \quad (3)$$

where $f_x = [DIC_x]/[DIC_{total}]$, the subscript x denotes either POCSR, AOM, and OLD, and $[DIC_{total}]$ equals to $[DIC_{meas}] + [DIC_{CARB}]$.

Using this approach and the first order estimates detailed in Section 4.2.1, we conclude that ca. 72% of the DIC at Site ARA06C-JPC01 is produced through AOM and POCSR, while the remaining 28% originates from the old DIC pool characterized by a heavy ^{13}C signature (+23‰).

In general, DIC enriched in ^{13}C points to the removal of light carbon in a closed marine system, possibly resulting from ME in sediments isolated from additional carbon input, which we postulate was provided by a pulse in subsurface fluid flow. This conclusion agrees with recent estimates that CH_4 in shallow Beaufort Sea sediments is being released from ancient carbon inventories that include permafrost and gas hydrate (Sparrow et al., 2018).

The estimates above are based on additional assumptions that the measured total alkalinity primarily consists of bicarbonate with a negligible contribution of hydrogen sulfide. Assuming bicarbonate as the sole constituent in the carbonate system is reasonable due to the slightly basic pore water. The assumption of no sulfide may be problematic as sulfide concentration can be as high as tens of mM in cold seep environments, but the proximity to land presumes enough iron to remove sulfides at our site, and furthermore, we did not detect a hydrogen sulfide smell during core sampling on the deck. If we assume an even lower $\delta^{13}C_{AOM\text{-}DIC}$ value, the isotopic signature for the old DIC would need to be higher to meet the mass balance requirement. Our assumption of no significant *in situ* CO_2 reduction, and the omission of the process in Equation 3, is supported by the absence of downcore changes below the SMT in the $\delta^{13}C_{DIC}$ profile (Figure 2; Table S1). From locations where *in situ* CO_2 reduction dominates CH_4 production, the residual DIC is enriched in ^{13}C as reflected by the positive $\delta^{13}C_{DIC}$ values (Kim, Torres, Lee, et al., 2013; Whiticar, 1999). This is however not the case for our records and suggests insignificant *in situ* CO_2 reduction for the investigated sites. This inference is further supported by the isotopic signatures from the dissolved CO_2 and CH_4 (see Section 4.2.3 for more details). Notwithstanding these potential errors, it is clear that a contribution from an old DIC pool is needed to explain its isotopic composition in the pore waters at Site ARA06C-JPC01.

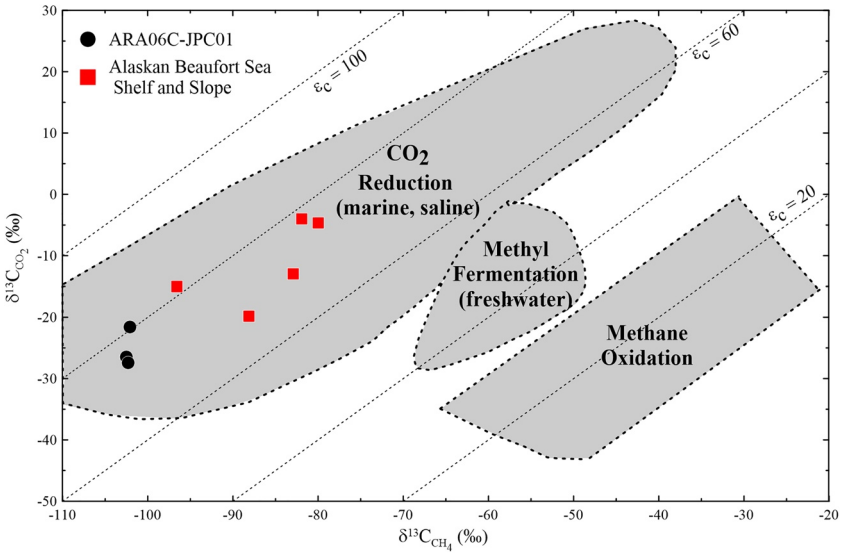

Figure 5. Paired values of $\delta^{13}C_{CH4}$ and $\delta^{13}C_{CO2}$ with isotopic fractionation lines (ε_c). All data from Site ARA06C-JPC01 (black closed circles) and the Alaskan Beaufort Sea and Shelf Slope (red closed squares) are in the region of CO_2 reduction pathway. The $\delta^{13}C_{CH4}$ and $\delta^{13}C_{CO2}$ data of the Alaskan Beaufort Sea Shelf and Slope are from Lorenson et al. (2016).

4.2.3. Methane and Dissolved Organic Matter

To provide further evidence for our inferences and evaluate the consequences of a DIC-enriched water pulse associated with subsurface discharge, we analyzed chemical and isotopic composition of dissolved gas samples from Site ARA06C-JPC01 and estimated carbon fractionation factor ($\varepsilon_c \approx \delta^{13}C_{CO2} - \delta^{13}C_{CH4}$). In addition, we compared our results with data from other cores in the Alaskan Beaufort Sea (Coffin et al., 2013; Lorenson et al., 2016) (Figures 2 and 5; Table S2).

The carbon fractionation factor ($\varepsilon_c \approx \delta^{13}C_{CO2} - \delta^{13}C_{CH4}$) is estimated by the difference between carbon isotopes of CH_4 and CO_2 that were produced and consumed, respectively, during the ME process (Kim et al., 2012; Pohlman et al., 2009; Whiticar, 1999). In marine environments associated with ME, ε_c values range between 49 to 100‰, with most commonly observed values associated with CO_2 reduction around 65–75‰ (Kim et al., 2012; Pohlman et al., 2009; Whiticar, 1999). The ε_c values at Site ARA06C-JPC01 range from 75 to 80‰ (Figure 5; Table S2), consistent with a microbial CH_4 origin via CO_2 reduction (Whiticar, 1999). These inferences are in agreement with CH_4 generation mechanisms previously reported for the shelf and slope of the Beaufort Sea (Coffin et al., 2013; Lorenson et al., 2016) (Figure 5).

Though we concluded that the CH_4 production occurred through CO_2 reduction, we note that the process did not occur *in situ* at Site ARA06C-JPC01, as revealed by the conversion ratios (r) we calculated using a simplified Rayleigh distillation function (Whiticar, 1999), defined by Equations 4 and 5.

$$\delta^{13}C_{CO2,t} = \delta^{13}C_{CO2,i} - \varepsilon_c ln\left(1-r\right) \tag{4}$$

$$\delta^{13}C_{CH4,t} = \delta^{13}C_{CO2,i} - \varepsilon_c \left(1 + ln\left(1-r\right)\right) \tag{5}$$

where $\delta^{13}C_{CO2,t}$ and $\delta^{13}C_{CH4,t}$ are the isotopic ratios of CO_2 and CH_4, respectively, at time t. $\delta^{13}C_{CO2,i}$ is the isotopic ratio of sedimentary organic matter at depth i, ε_c is fractionation factor between CO_2 and CH_4, and $1 - r$ is the remaining fraction of the initial substrate.

If we assume that a carbon isotopic ratio of −24‰ reflects organic matter delivered to Site ARA06C-JPC01, the estimated conversion factor between CH_4 and CO_2 is <2%. This factor is much lower than that estimated for the Beaufort Sea, which ranges between 6% and 23% (average = 15%, $n = 5$) (Lorenson et al., 2016). Alternatively, to assign a conversion factor of 15% to the sediment at Site ARA06C-JPC01, consistent with

other sites in the region, would necessitate the organic matter to have an isotopic ratio lower than −35%, which is unreasonably low for either terrestrial or marine sources. We conclude that CH_4 was not generated via *in situ* CO_2 reduction fueled by the degradation of local organic carbon at Site ARA06C-JPC01. Instead, there must be substantial contribution of allochthonous CH_4, supplied by the subsurface flow pulse.

The postulated subsurface flow would also affect inventories of dissolved organic matter (DOM) in the coastal area of the Arctic Ocean, as documented by previous research that conducted fluorescent dissolved organic matter (FDOM) measurements at our study sites (Chen et al., 2016). These authors show that Site ARA06C-JPC01 has the highest abundance of a terrestrial humic-like FDOM among all the sites sampled during the ARA06C Expedition. Such FDOM characteristics are generally reported in coastal wetland ecosystems, and in canal waters that drain agricultural areas with peat-derived DOM (Yamashita et al., 2010). These findings are consistent with our inference that pore water data from Site ARA06C-JPC01 reflect input from a fluid source modified during its transport and carbon remobilization from old organic matter sequences.

4.3. Subsurface Flow Inferred From Trace Element Compositions in the Pore Water

The postulated subsurface flow not only has an impact on the dissolved carbon species at Site ARA06C-JPC01, but also changes the trace element compositions and the corresponding isotopic signatures of the pore waters. Compared to the other study sites, pore waters from Site ARA06C-JPC01 are enriched in Ba^{2+} and B as well as carrying signatures of low $\delta^{11}B$ and high $^{87}Sr/^{86}Sr$ (Figure 2; Table S1).

The $\delta^{11}B$ data at Site ARA06C-JPC01 range from +20.5‰ to +35.1‰, which are significantly lower than that of seawater (+39.6‰) and those in pore waters from Site ARA06C-JPC04 (+38.0 ± 2.5‰) (Table S1). Moreover, the sample displaying the lowest $\delta^{11}B$ at Site ARA06C-JPC01 corresponds to the depth of maximum CH_4 concentration (Tables S1 and S2); although we recognize the sparsity of $\delta^{11}B$ analyses relative to the CH_4 data. During early diagenesis in marine sediment, organic matter degradation may lead to an increase in B concentration with enriched ^{10}B through NH_4^+ exchange (Teichert et al., 2005). However, this is not the case for Site ARA06C-JPC01 as there is no correlation between NH_4^+ concentration and either B concentration or $\delta^{11}B$ value (Figure S2; Table S1). Alternatively, we argue that the anomalously low $\delta^{11}B$ values in pore waters at Site ARA06C-JPC01 are consistent with a late-stage release of isotopically light B from old organic carbon reservoirs. Williams et al. (2001) show that B released during the late-stages of organic matter degradation could have a distinctly negative $\delta^{11}B$. For example, $\delta^{11}B$ value as low as ∼17‰ has been reported from the water in oilfields of the Gulf Coast basins, USA. Similarly, low $\delta^{11}B$ in groundwater discharge with increasing B concentration has been attributed to release from organic matter (Barth, 2000). The inference made from pore water boron systematics is in agreement with observations from $\delta^{13}C_{DIC}$ and published FDOM characteristics at the same site (Chen et al., 2016).

The observed high concentration of Ba^{2+} in the pore waters also supports subsurface flow as a freshened fluid source at Site ARA06C-JPC01. Whereas we cannot negate the possibility that high Ba^{2+} originates by barite dissolution below the SMT (Torres et al., 1996), the elevated Ba^{2+} concentration is consistent with that expected in subsurface fluid devoid of SO_4^{2-}, given the high concentration of Ba^{2+} in riverine waters discharging into the Arctic Ocean from surface weathering of rocks in the region (Guay & Falkner, 1998). Hong et al. (2019) recently reported up to ∼1 mM dissolved Ba^{2+} at a cold seep, which they interpreted as resulting from subsurface groundwater discharge along northern Norwegian margin, similar to our postulated scenario for the high barium observation at the Chukchi Sea Shelf (Figure 2; Table S1). The observed high H_4SiO_4 concentration (Figure 2; Table S1) in the pore waters at Site ARA06C-JPC01 likely reflects weathering processes in the subsurface and explains the radiogenic strontium signature in pore waters. In contrast, decreasing $^{87}Sr/^{86}Sr$ values with depth in pore waters from Sites ARA06C-JPC02, ARA06C-JPC03, and ARA06C-JPC-04 (Figure 2; Table S1) reflect the contribution of diagenetic alteration of detrital carbonate and/or volcanogenic facies in the sediments (Teichert et al., 2005).

In summary, whereas each of the observations detailed thus far with their associated uncertainties, individually may be considered a weak argument, collectively the suite of pore water and dissolved gas data from Site ARA06C-JPC01 provide strong evidence for the presence of a subsurface flow of freshened fluids with a meteoric water signal that drains old organic carbon deposits and weathers the underlying continental

crust. In so, this subsurface flow delivered fluids with distinct and anomalous composition to the shelf region of the Chukchi Sea.

4.4. Establishing a Time Frame for the Subsurface Flow

The outstanding issue we need to resolve is the timing for the postulated subsurface flow discharge, which would help determine the drivers of flow. The model we used to constrain the carbon sources in Section 4.2, points to a system that has reached a quasi-steady state condition. As previously shown in other regions, changes in the CH_4 supply result in SO_4^{2-} profiles with distinct concave-up or concave-down curvatures (e.g., Fischer et al., 2013; Hong et al., 2017). The profiles of our pore water data are thus not consistent with a recent CH_4 pulse, which may have been triggered by anthropogenically induced permafrost degradation. To better determine whether and when the CH_4 pulse occurred, we used a numerical model modified from the one established by Hong et al. (2017) to evaluate how the SO_4^{2-} profile at Site ARA06C-JPC01 may have evolved under different scenarios of CH_4 supply. In other words, we synthetically changed the CH_4 input component to observe the predicted shape of the SO_4^{2-} profiles at different time frames. Because we do not have any constraints on the past composition of the discharging fluids, nor the reactivity or metabolic pathways modifying organic carbon in the past, the model was targeted to only simulate the SO_4^{2-} response to a CH_4 pulse by only considering changes in SO_4^{2-} and CH_4 and assuming AOM as the only SO_4^{2-} sink.

We first simulated three scenarios with different levels of CH_4 input, by assigning 5, 50, and 500 mM as the lower boundary CH_4 condition while assigning SO_4^{2-} concentration as zero in the bottom cell of all scenarios. The assigned CH_4 bottom boundary conditions do not represent realistic concentrations observed in the sediments, as gas hydrate formation takes place when CH_4 concentration is over ca. 60 mM for the water depth at our investigated site (gas hydrate is not included in the model). Rather, these concentrations are meant to reproduce the different end-member CH_4 fluxes at depth to investigate the responses of downcore SO_4^{2-} profiles. For the top boundary condition, we assigned 0 and 29 mM for CH_4 and SO_4^{2-}, respectively. We assumed that once the CH_4 reaches the core location, diffusion is the only solute transport mechanism and assigned diffusion coefficients for SO_4^{2-} and CH_4 of 0.0065 and 0.0123 m^2/yr, assuming a constant porosity of 0.7.

None of these scenarios can fit the observations (Figures 6a–6c). This is not surprising since systems that are characterized by a recent increase in CH_4 display concave-up SO_4^{2-} profiles that are entirely different from what we have observed at Site ARA06C-JPC01. Such a concave-up SO_4^{2-} profile has been shown from offshore Makran, which reflects a recent CH_4 increase attributed to the 1945 earthquake in the region (Fischer et al., 2013).

To explain the observed SO_4^{2-} profile, we therefore added one additional scenario, where the CH_4 supply at Site ARA06C-JPC01 was terminated after an initially large CH_4 pulse. In this scenario, we used the modeled SO_4^{2-} and CH_4 profiles in the "high-flux" scenario as the initial condition (2,500 year in Figure 6b) and assigned a zero CH_4 concentration as the lower boundary condition representing a scenario that CH_4 supply was suddenly terminated at the bottom of the core. Since there is still residual dissolved CH_4 in the pore space that could sustain some activities of AOM, the SMT depth did not change drastically in the first 1,500 years. Gradually, the exhaustion of CH_4 deepens the SMT and results in the observed concave-down SO_4^{2-} profile at ca. 2,800 years after the initial condition (Figure 6d).

We recognize here some uncertainties resulting from our approach, particularly the assumption that all SO_4^{2-} is consumed by AOM, in light that we have shown that at present ~30% of the SO_4^{2-} is consumed by organic matter through POCSR, and ~70% is consumed by AOM. However, given that: (a) organic carbon input to the sediment at Site ARA06C-JPC01 has remained approximately constant in the past ~8 ka BP at ~1.8 wt.% (Figure S1; Table S3); and (b) the site has experienced fluid advection of CH_4 rich fluids, which occurs at rates faster than any changes in POCSR, especially given the relatively slow sediment deposition (e.g., 0.091 cm/yr as calculated from the sediment age) (Figure S1), we argue that the current model setup and the associated assumption of no POCSR are sufficient to derive a first order approximation for the timing of the fluid seepage event. We also note here that, due to the assumption of no POCSR, an excellent fit with the data is not possible. We aim only to investigate how the slightly concave-down SO_4^{2-} profile

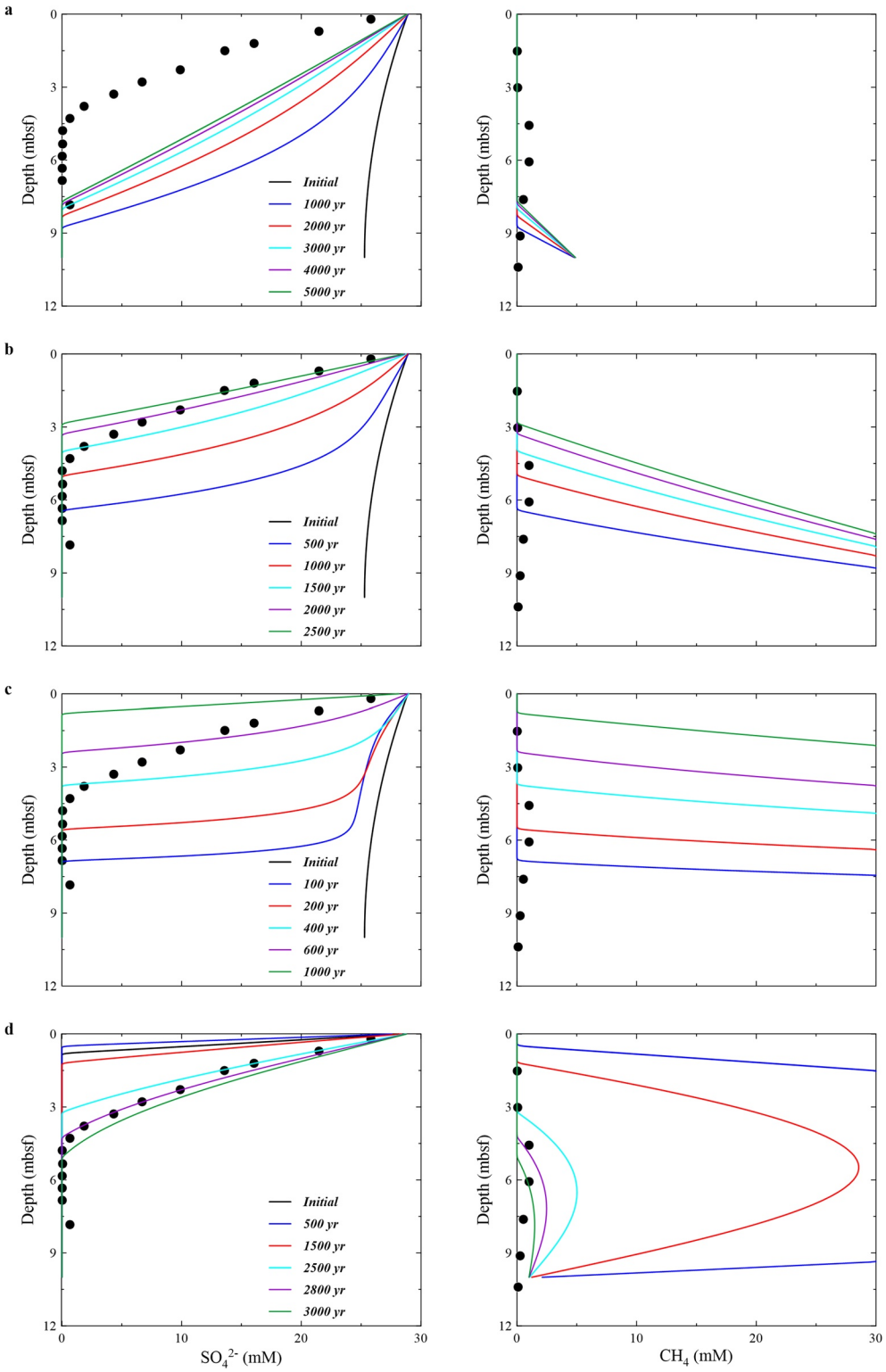
a
b
c
d
Depth (mbsf)
Initial
1000 yr
2000 yr
3000 yr
4000 yr
5000 yr
500 yr
1500 yr
2500 yr
100 yr
200 yr
400 yr
600 yr
2800 yr
SO_4^{2-} (mM)
CH_4 (mM)

Figure 6.

(Figure 6), could occur under the different CH_4 fluxes and time scales, and clearly show that the associated CH_4 pulse is not related to anthropogenic forcings.

We also note that our model can only constrain the minimum duration of time needed to generate the observed profiles, since the simulation assumes the CH_4 supply was suddenly terminated by assigning a zero CH_4 concentration at the bottom of the core. It is therefore likely that it took more than 2.8 kyrs after the cessation of the CH_4 pulse for the system to reach the condition reflected in the current pore water profile. In addition, we are uncertain whether the pore water system is currently in a steady state or approaching one. The latter may be more likely, or the pore water system is still readjusting after the proposed disturbance as assigned in our numerical model. Nonetheless, these simulations clearly show that a CH_4 increase driven by anthropogenic warming over the past centuries is unlikely to explain SO_4^{2-} profile at Site ARA06C-JPC01 as it takes more than a few hundred years to shoal the SMT from >10 mbsf to the current depth (Figure 6).

4.5. Paleoenvironmental Setting

To interpret our results in the context of paleoceanographic conditions at our study site, we rely on data and inferences derived from Site ARA06C-JPC01, recovered ~3 km from Site ARA2B-1A (Stein et al., 2017) (Figure 1; Figure S1). Based on a correlation of magnetic susceptibility and wet bulk density between Sites ARA06C-JPC01 and ARA2B-1A (Figure S1), we assign an age of ~8.1 ka BP to ~6.1 mbsf sediment in Site ARA06C-JPC01 (Figure S1), corresponding to the timing of EHTM. During the LGM, the global sea level was 120 m lower than the present, therefore Site ARA06C-JPC01 was close to/or above sea level at that time. Since present permafrost coverage in the Beaufort Sea extends to the 25 m isobath (Brothers et al., 2016), it is also likely that Site ARA06C-JPC01 was covered by permafrost during the LGM (Figure 1). Because of the shallow water conditions during the LGM, Site ARA06C-JPC01 was subject to the input of organic matter from terrestrial sources. As sea level and temperature increased during deglaciation, ice coverage at Site ARA06C-JPC01 reached a minimum level during the EHTM (Wanner et al., 2008). During this time frame, where insulation increased and temperature increased by 2–3°C, it is likely that thawing of permafrost triggered the freshwater pulse we see now in our pore water data.

4.6. Postulated Scenario and Mechanisms Driving the Subsurface Flow

Based on our collective results, and in the context of available paleoceanographic reconstruction (Stein et al., 2017), we postulate a scenario that calls for an anomalous increase in subsurface flow at the onset of the EHTM (Figure 7; Figure S1). It is possible that the 2–3°C warming experienced in this region during the EHTM (Renssen et al., 2009; Stein et al., 2017), may have led to rapid permafrost thawing and enhanced subsurface flow towards the coastal Arctic, similar to the flow predicted by hydrologic projections and climate models associated with the disappearance of the Laurentide Ice Sheet (Renssen et al., 2009).

The landmasses surrounded the Arctic host sediments are rich in old organic matter. In our scenario, remineralization of this carbon in a closed subsurface reservoir (Mann et al., 2010) produced fluids with ^{13}C-depleted CH_4 and ^{13}C-enriched DIC. Water migration transported DOM (as shown by Chen et al., 2016), CH_4, and DIC (as shown here) previously trapped in or beneath the permafrost. Degradation of ancient organic carbon, perhaps subsurface peat, also supplies B enriched in ^{10}B. In summary, these conditions result in the highly ^{13}C-depleted CH_4 pool, ^{13}C-enriched DIC, humic-like FDOM, and a depleted $\delta^{11}B$ signal, currently sampled at the Site ARA06C-JPC01 (Chen et al., 2016; Figure 2; Tables S1 and S2). We recognize that the hydrological mechanisms supporting flow are at this point highly unconstrained. Nonetheless, based on

Figure 6. Model results for the three different scenarios of (a) low (5 mM), (b) medium (50 mM), and (c) high (500 mM) in CH_4 supply, which show different sulfate-methane transition (SMT) shoaling rates. With a low CH_4 supply, it takes 3 kyrs for the SMT to shoal 8 mbsf; for the medium CH_4 supply, it takes 1.5 kys for the SMT to shoal 4 mbsf; for the high CH_4 supply, it takes only 600 years for the SMT to shoal 2.5 mbsf. It is also observed that, with increasing CH_4 supply, the SO_4^{2-} profiles tend to exhibit the non-steady state with concave-up profiles; this is apparently different from the observed concave-down SO_4^{2-} profile. (d) Model result for a scenario with decreasing CH_4 supply following cessation of fluid input. The initial condition of this scenario has very shallow SMT (ca. 1.0 mbsf) and the lower boundary condition of CH_4 is set to be zero. The fluid system evolves without a new supply of CH_4 from the bottom of the core. As a result, the SMT gradually deepens as CH_4 in the sediment column is consumed through anaerobic oxidation of methane (AOM). It takes ca. 2.8 kyrs for the modeled SO_4^{2-} profile to fit the current observation.

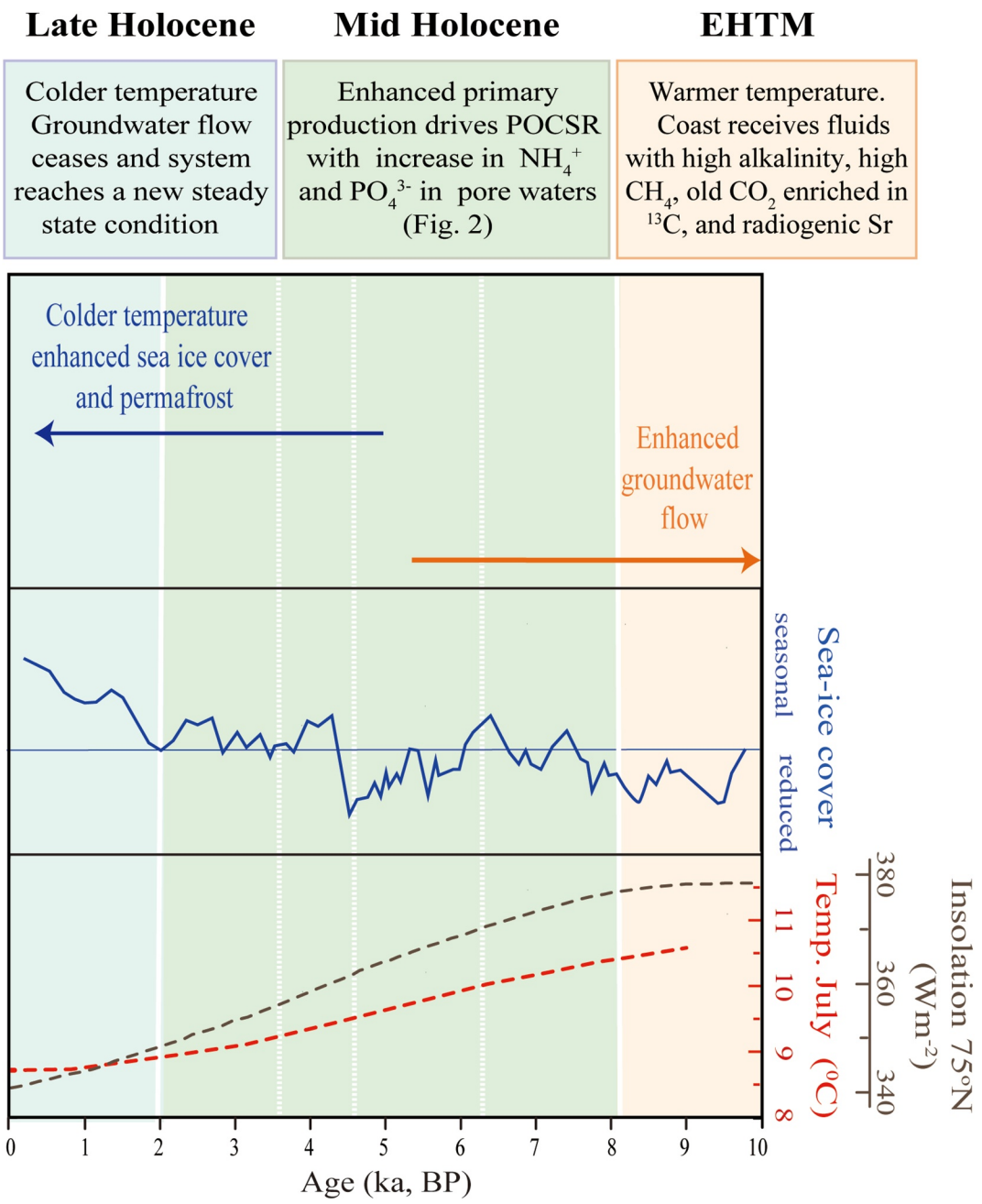

Figure 7. Schematic diagram illustrating the evolution in sea ice coverage (from PIP_{25} estimates from Stein et al. (2017) shown in blue) experienced at Site ARA06C-JPC01, based on data for a near-by core collected by Stein et al. (2017). The dotted red line indicates July temperature estimates of Renssen et al. (2009), which result from an increase in solar insolation plotted as a black curve in Stein et al. (2017). Based on comparison from these results, our geochemical data and numerical simulation propose a change from a system influenced by subsurface flow that reached the Arctic coast during the Early Holocene Thermal Maximum (EHTM), followed by cessation of flow as temperature decreased, overlaid by an increase in primary production during the middle Holocene.

the preponderance of geochemical evidence, we postulate that the permafrost thawing drove subsurface flow of CH_4-enriched water in the Chukchi coastal area was triggered by warming during the EHTM (Figure 7). The flow was likely terminated at 4 ka BP due to the onset of cold temperature and consequential permafrost formation (Figure 7). The decreasing supply of CH_4 could no longer sustain the high AOM activities during the initial CH_4 pulse and resulted in the deepened SMT as demonstrated in our last modeling

scenario (Figure 6d). The current concave-down SO_4^{2-} profile at Site ARA06C-JPC01 reflects such a signal that takes >2.8 kyr to evolve after the termination of CH_4 seepage.

5. Conclusions and Implications

Chloride concentration and water isotope data delineate the occurrence of freshwater discharge in the Chukchi Sea Shelf. Our observations expand the freshening area in the Chukchi Sea as far as 300 km from shore, distinct from the scenarios thus far discussed for offshore freshwaters in this area. At present, vast emplacements of offshore freshwaters worldwide have been attributed to freshwater infiltration during low sea level periods throughout the Pliocene and Pleistocene (Post et al., 2013). Our proposed scenario suggests that freshening in the Arctic region may also have occurred by permafrost thawing in response to warming following the LGM, specifically during the ETHM.

The concentration and isotopic characteristics of various carbon species (DIC, CH_4, and DOM) reveal the intensive alteration of organic carbon on land, possibly in a closed system. The light $\delta^{11}B$ signal is also consistent with the ^{10}B release from ancient organic carbon reservoirs (Williams et al., 2001). The migrating fluids would weather rock formations, remobilizing H_4SiO_4, Ba^{2+}, and other ions, and imparting an enriched $^{87}Sr/^{86}Sr$ fingerprint to the fluids (Figures 2, 4, and 7). Input of metals and dissolved carbon via subsurface discharge are important components of the mass fluxes in the coastal areas, and have been reported in the fluids from the French Mediterranean, Florida, Baltic Sea, and other margins (Martin et al., 2007; Oehler et al., 2017). Our data provide another example of land-ocean connections, and significantly expand previous observations reported along the Beaufort Sea.

Global climate change impacts the hydrology of the permafrost-covered region in the Arctic areas (Figure 7). A review of recent studies investigating linkages between permafrost dynamics and river biogeochemistry in the Arctic, forecasts a transition from a mineral-poor surface water-dominated system to a mineral-rich groundwater-dominated system, with an associated increase in major ions, PO_4^{3-}, and H_4SiO_4 export to the coastal area (Colombo et al., 2018; Frey & McClelland, 2009). To cite a specific example, change in temperature, precipitation, and permafrost degradation have enhanced rock weathering and sulfide oxidation throughout the Yukon River Basin, as evidenced by changes in river fluxes of Ca^{2+}, Mg^{2+}, Na^+, SO_4^{2-}, and PO_4^{3-} (Toohey et al., 2016). These predictions do not provide information as to whether the amount and nature of the carbon species reaching the coastal waters will increase or decrease with warming and permafrost thawing. Our data from Site ARA06C-JPC01, indicate that enhanced subsurface fluid migration could deliver significant amounts of carbon, in the form of CH_4, DOM, and DIC to the coastal area (Figures 4, 6, and 7).

If our observations reflect an increase in water and CH_4 discharge to the coastal Arctic as a response to the 2–3°C increase in temperature at the EHTM, the fact that the subsurface discharge occurred in the shallow shelf region suggests the possibility of CH_4 contribution to the atmosphere (Yang et al., 2017). Our results complement other studies of predicted changes in the hydrological regime of Arctic regions as our planet warms, which indicate a significant increase in the delivery of dissolved species via subsurface discharge with important implications for element budgets and carbon cycling along the Arctic shelves.

Future studies targeting land-to-sea processes in the Arctic Ocean, and the roles that hydrography, fluid source regions, and subsurface lithology have on subsurface flow are needed to unravel crucial factors for understanding the response of the system through geological time and for predicting future effects of climate change on biogeochemical element cycling in general, and the carbon cycle in particular.

Data Availability Statement

Data used in this research have been in the Supporting Information of this paper and are available on https://doi.pangaea.de/10.1594/PANGAEA.933597.

Acknowledgments
We would like to thank the shipboard scientific party, captain, and crew of the *IBRV ARAON* during the *IBRV* ARAON Arctic Expedition in 2015 (ARA06C). This work was supported by the Korea Ministry of Science and ICT (GP2020-038), by the Korea Ministry of Oceans and Fisheries (NP2011-040 and 1525011795), and by the Korea Polar Research Institute (Grants No. PE20350). W.-L. Hong acknowledges the supports from the ArcticSGD, a project supported by the Norway Grants and the EEA Grants (2019/34/H/ST10/00645). Additional funds were contributed by the AWI Research Program PACES-II Workpackage 3.1 and 3.2.

References

Barth, S. R. (2000). Stable isotope geochemistry of sediment-hosted groundwater from a Late Paleozoic-Early Mesozoic section in central Europe. *Journal of Hydrology*, *235*, 72–87. https://doi.org/10.1016/s0022-1694(00)00264-x

Bense, V. F., Ferguson, G., & Kooi, H. (2009). Evolution of shallow groundwater flow systems in areas of degrading permafrost. *Geophysical Research Letters*, *36*, L22401. https://doi.org/10.1029/2009GL039225

Brothers, L. L., Herman, B. M., Hart, P. E., & Ruppel, C. D. (2016). Subsea ice-bearing permafrost on the U.S. Beaufort Margin: 1. Minimum seaward extent defined from multichannel seismic reflection data. *Geochemistry, Geophysics, Geosystems*, *17*, 4354–4365. https://doi.org/10.1002/2016GC006584

Chatterjee, S., Dickens, G. R., Bhatnagar, G., Chapman, W. G., Dugan, B., Snyder, G. T., & Hirasaki, G. J. (2011). Pore water sulfate, alkalinity, and carbon isotope profiles in shallow sediment above marine gas hydrate systems: A numerical modeling perspective. *Journal of Geophysical Research*, *116*, B09103. https://doi.org/10.1029/2011JB008290

Chen, M., Kim, J.-H., Nam, S.-I., Niessen, F., Hong, W. L., Kang, M.-H., & Hur, J. (2016). Production of fluorescent dissolved organic matter in Arctic Ocean sediments. *Scientific Reports*, *6*, 39213. https://doi.org/10.1038/srep39213

Christensen, T. R., Johansson, T., Åkerman, H. J., Mastepanov, M., Malmer, N., Friborg, T., et al. (2004). Thawing sub-arctic permafrost: Effects on vegetation and methane emissions. *Geophysical Research Letters*, *31*, L04501. https://doi.org/10.1029/2003GL018680

Coffin, R. B., Smith, J. P., Plummer, R. E., Yoza, B., Larsen, R. K., Millholland, L. C., & Montgomery, M. T. (2013). Spatial variation in shallow sediment methane sources and cycling on the Alaskan Beaufort Sea Shelf/Slope. *Marine and Petroleum Geology*, *45*, 186–197. https://doi.org/10.1016/j.marpetgeo.2013.05.002

Colombo, N., Salerno, F., Gruber, S., Freppaz, M., Williams, M., Fratianni, S., & Giardino, M. (2018). Review: Impacts of permafrost degradation on inorganic chemistry of surface fresh water. *Global and Planetary Change*, *162*, 69–83. https://doi.org/10.1016/j.gloplacha.2017.11.017

Craig, H. (1961). Isotopic variation in meteoric waters. *Science*, *133*, 1702–1703. https://doi.org/10.1126/science.133.3465.1702

Dove, D., Polyak, L., & Coakley, B. (2014). Widespread, multi-source glacial erosion on the Chukchi margin, Arctic Ocean. *Quaternary Science Reviews*, *92*, 112–122. https://doi.org/10.1016/j.quascirev.2013.07.016

Fischer, D., Mogollón, J. M., Strasser, M., Pape, T., Bohrmann, G., Fekete, N., et al. (2013). Subduction zone earthquake as potential trigger of submarine hydrocarbon seepage. *Nature Geoscience*, *6*, 647–651. https://doi.org/10.1038/ngeo1886

Frey, K. E., & McClelland, J. W. (2009). Impacts of permafrost degradation on arctic river biogeochemistry. *Hydrological Processes*, *23*, 169–182. https://doi.org/10.1002/hyp.7196

Fritz, M., Wetterich, S., Meyer, H., Schirrmeister, L., Lantuit, H., & Pollard, W. H. (2011). Origin and characteristics of massive ground ice on Herschel Island (western Canadian Arctic) as revealed by stable water isotope and hydrochemical signatures. *Permafrost and Periglacial Processes*, *22*, 26–38. https://doi.org/10.1002/ppp.714

Garcia-Tigreros Kodovska, F., Sparrow, K. J., Yvon-Lewis, S. A., Paytan, A., Dimova, N. T., Lecher, A., & Kessler, J. D. (2016). Dissolved methane and carbon dioxide fluxes in Subarctic and Arctic regions: Assessing measurement techniques and spatial gradients. *Earth and Planetary Science Letters*, *436*, 43–55. https://doi.org/10.1016/j.epsl.2015.12.002

Guay, C. K., & Falkner, K. K. (1998). A survey of dissolved barium in the estuaries of major Arctic rivers and adjacent seas. *Continental Shelf Research*, *18*, 859–882. https://doi.org/10.1016/s0278-4343(98)00023-5

Gwiazda, R., Paull, C. K., Dallimore, S. R., Melling, H., Jin, Y. K., Hong, J. K., et al. (2018). Freshwater seepage into sediments of the shelf, shelf edge, and continental slope of the Canadian. *Geochemistry, Geophysics, Geosystems*, *19*, 3039–3055. https://doi.org/10.1029/2018GC007623

Hong, W.-L., Lepland, A., Himmler, T., Kim, J.-H., Chand, S., Sahy, D., et al. (2019). Discharge of meteoric water in the eastern Norwegian Sea since the last glacial period. *Geophysical Research Letters*, *46*, 8194–8204. https://doi.org/10.1029/2019GL084237

Hong, W.-L., Sauer, S., Panierei, G., Ambrose, W. G., Jr, James, R. H., Plaza-Faverolar, A., & Schneider, A. (2016). Removal of methane through hydrological, microbial, and geochemical processes in the shallow sediments of pockmarks along eastern Vestnesa Ridge (Svalbard). *Limnology and Oceanography*, *61*, S324–S343. https://doi.org/10.1002/lno.10299

Hong, W.-L., Torres, M. E., Carroll, J., Crémière, A., Panierei, G., Yao, H., & Serov, P. (2017). Seepage from an Arctic shallow marine gas hydrate reservoir is insensitive to momentary ocean warming. *Nature Communications*, *8*, 15745. https://doi.org/10.1038/ncomms15745

Jakobsson, M. (2002). Hypsometry and volume of the Arctic Ocean and its constituent seas. *Geochemistry, Geophysics, Geosystems*, *3*, 1–18. https://doi.org/10.1029/2001GC000302

Jakobsson, M., Andreassen, K., Bjarnadóttir, L. R., Dove, D., Dowdeswell, J. A., England, J. H., et al. (2014). Arctic Ocean glacial history. *Quaternary Science Reviews*, *92*, 40–67. https://doi.org/10.1016/j.quascirev.2013.07.033

Kastner, M., Elderfield, H., & Martin, J. B. (1991). Fluids in convergent margins: What do we know about their composition, origin, role in diagenesis and importance for oceanic chemical fluxes? *Philosophical Transactions of the Royal Society A: Mathematical, Physical and Engineering Sciences*, *335*, 243–259. https://doi.org/10.1098/rsta.1991.0045

Kim, J.-H., Hachikubo, A., Kida, M., Minami, H., Lee, D.-H., Jin, Y. K., et al. (2020). Upwarding gas source and postgenetic processes in the shallow sediments from the ARAON Mounds, Chukchi Sea. *Journal of Natural Gas Science and Engineering*, *76*, 103223. https://doi.org/10.1016/j.jngse.2020.103223

Kim, J.-H., Torres, M. E., Choi, J., Bahk, J.-J., Park, M.-H., & Hong, W.-L. (2012). Inferences on gas transport based on molecular and isotopic signatures of gases at acoustic chimneys and background sites in the Ulleung Basin. *Organic Geochemistry*, *43*, 26–38. https://doi.org/10.1016/j.orggeochem.2011.11.004

Kim, J.-H., Torres, M. E., Hong, W.-L., Choi, J., Riedel, M., Bahk, J.-J., & Kim, S. H. (2013). Pore fluid chemistry from the second gas hydrate drilling expedition in the Ulleung Basin (UBGH2): Source, mechanisms and consequences of fluid freshening in the central part of the Ulleung Basin, East Sea. *Marine and Petroleum Geology*, *47*, 99–112. https://doi.org/10.1016/j.marpetgeo.2012.12.011

Kim, J.-H., Torres, M. E., Lee, J.-Y., Hong, W.-L., Holland, M., Park, M.-H., et al. (2013). Depressurization experiment of pressure cores from the central Ulleung Basin, East Sea: Insights into gas chemistry. *Organic Geochemistry*, *62*, 86–95. https://doi.org/10.1016/j.orggeochem.2013.07.010

Lapham, L., Marshall, K., Magen, C., Lyubchich, V., Cooper, L. W., & Grebmeier, J. M. (2017). Dissolved methane concentrations in the water column and surface sediments of Hanna Shoal and Barrow Canyon, Northern Chukchi Sea. *Deep-Sea Research Part II: Topical Studies in Oceanography*, *144*, 92–103. https://doi.org/10.1016/j.dsr2.2017.01.004

Lecher, A. L., Kessler, J., Sparrow, K., Garcia-Tigreros Kodovska, F., Dimova, N., Murray, J., et al. (2016). Methane transport through submarine groundwater discharge to the North Pacific and Arctic Ocean at two Alaskan sites. *Limnology and Oceanography*, *61*, S344–S355. https://doi.org/10.1002/lno.10118

Lorenson, T. D., Greinert, J., & Coffin, R. B. (2016). Dissolved methane in the Beaufort Sea and the Arctic Ocean, 1992-2009; sources and atmospheric flux. *Limnology and Oceanography*, *61*, S300–S323. https://doi.org/10.1002/lno.10457

Mann, D. H., Groves, P., Reanier, R. E., & Kunz, M. L. (2010). Floodplains, permafrost, cottonwood trees, and peat: What happened the last time climate warmed suddenly in arctic Alaska? *Quaternary Science Reviews*, *29*, 3812–3830. https://doi.org/10.1016/j.quascirev.2010.09.002

Martin, J. B., Cable, J. E., Smith, C., Roy, M., & Cherrier, J. (2007). Magnitudes of submarine groundwater discharge from marine and terrestrial sources: Indian River Lagoon, Florida. *Water Resources Research*, *43*, W05440. https://doi.org/10.1029/2006WR005266

Niessen, F., Hong, J. K., Hegewald, A., Matthiessen, J., Stein, R., Kim, H., et al. (2013). Repeated Pleistocene glaciation of the East Siberian continental margin. *Nature Geoscience*, *6*, 842–846. https://doi.org/10.1038/ngeo1904

Oehler, T., Mogoll, J. M., Moosdorf, N., Winkler, A., Kopf, A., & Pichler, T. (2017). Submarine groundwater discharge within a landslide scar at the French Mediterranean coast. *Estuarine, Coastal and Shelf Science*, *198*, 128–137. https://doi.org/10.1016/j.ecss.2017.09.006

Pados, T., Spielhagen, R. F., Bauch, D., Meyer, H. M., & Segl, M. (2015). Oxygen and carbon isotope composition of modern planktic foraminifera and near-surface waters in the Fram Strait (Arctic Ocean) - A case study. *Biogeosciences*, *12*, 1733–1752. https://doi.org/10.5194/bg-12-1733-2015

Paull, C. K., Dallimore, S. R., Caress, D. W., Gwiazda, R., Melling, H., Riedel, M., et al. (2015). Active mud volcanoes on the continental slope of the Canadian Beaufort Sea. *Geochemistry, Geophysics, Geosystems*, *16*, 3160–3181. https://doi.org/10.1002/2015GC005928

Pohlman, J. W., Kaneko, M., Heuer, V. B., Coffin, R. B., & Whiticar, M. (2009). Methane sources and production in the northern Cascadia margin gas hydrate system. *Earth and Planetary Science Letters*, *287*, 504–512. https://doi.org/10.1016/j.epsl.2009.08.037

Polyak, L. V., Darby, D. A., Bischoff, J. F., & Jakobsson, M. (2007). Stratigraphic constraints on late Pleistocene glacial erosion and deglaciation of the Chukchi margin, Arctic Ocean. *Quaternary Research*, *67*, 234–245. https://doi.org/10.1016/j.yqres.2006.08.001

Post, V. E. A., Groen, J., Kooi, H., Person, M., Ge, S., & Edmunds, W. M. (2013). Offshore fresh groundwater reserves as a global phenomenon. *Nature*, *504*, 71–78. https://doi.org/10.1038/nature12858

Rae, J. W. B., Foster, G. V., Schmidt, D. N., & Elliott, T. (2011). Boron isotopes and B/Ca in benthic foraminifera: Proxies for the deep ocean carbonate system. *Earth and Planetary Science Letters*, *302*, 403–413. https://doi.org/10.1016/j.epsl.2010.12.034

Renssen, H., Seppä, H., Heiri, O., Roche, D. M., Goosse, G., & Fichefet, T. (2009). The spatial and temporal complexity of the Holocene thermal maximum. *Nature Geoscience*, *2*, 411–414. https://doi.org/10.1038/ngeo513

Riedel, M., Collett, T. S., Malone, M. J., & the Expedition 311 Scientists. (2006). Proceeding of the integrated ocean drilling program (Vol. 311). Washington, DC: Integrated Ocean Drilling Program Management International, Inc. https://doi.org/10.2204/iodp.proc.311.2006

Schuur, E. A. G., McGuire, A. D., Schädel, C., Grosse, G., Harden, J. W., Hayes, D. J., et al. (2015). Climate change and the permafrost carbon feedback. *Nature*, *520*, 171–179. https://doi.org/10.1038/nature14338

Smith, L. C., Sheng, Y., MacDonald, G. M., & Hinzman, L. D. (2005). Disappearing Arctic lakes. *Science*, *308*, 1429. https://doi.org/10.1126/science.1108142

Sparrow, K. J., Kessler, J. D., Southon, J. R., Garcia-Tigreros, F., Schreiner, K. M., Ruppel, C. D., et al. (2018). Limited contribution of ancient methane to surface waters of the U.S. Beaufort Sea shelf. *Sciences Advances*, *4*, eaao4882. https://doi.org/10.1126/sciadv.aao4842

Steefel, C., Appelo, C. A. J., Arora, B., Jacques, D., Kalbacher, T., Kolditz, O., et al. (2015). Reactive transport codes for subsurface environmental simulation. *Computers & Geosciences*, *19*, 445–478. https://doi.org/10.1007/s10596-014-9443-x

Stein, R., Fahl, K., Schade, I., Manerung, A., Wassmuth, S., Niessen, F., & Nam, S.-I. (2017). Holocene variability in sea ice cover, primary production, and Pacific-Water inflow and climate change in the Chukchi and East Siberian Seas (Arctic Ocean). *Journal of Quaternary Science*, *32*, 362–379. https://doi.org/10.1002/jqs.2929

Teichert, B. M. A., Torres, M. E., Bohrmann, G., & Eisenhauer, A. (2005). Fluid sources, fluid pathways and diagenetic reactions across an accretionary prism revealed by Sr and B geochemistry. *Earth and Planetary Science Letters*, *239*, 106–121. https://doi.org/10.1016/j.epsl.2005.08.002

Toohey, R. C., Herman-Mercer, N. M., Schuster, P. F., Mutter, E., & Koch, J. C. (2016). Multidecadal increases in the Yukon River Basin of chemical fluxes as indicators of changing flowpaths, groundwater, and permafrost. *Geophysical Research Letters*, *43*, 12120–12130. https://doi.org/10.1002/2016GL070817

Torres, M. E., Brumsack, H. J., Bohrmann, G., & Emeis, K.-C. (1996). Barite fronts in continental margin sediments: A new look at barium mobilization in the zone of sulfate reduction and formation of heavy barites in diagenetic fronts. *Chemical Geology*, *127*, 125–139. https://doi.org/10.1016/0009-2541(95)00090-9

Wanner, H., Beer, J., Bütikofer, J., Crowley, T. J., Cubasch, U., Flückiger, J., et al. (2008). Mid- to late Holocene climate change: An overview. *Quaternary Science Reviews*, *27*, 1791–1828. https://doi.org/10.1016/j.quascirev.2008.06.013

Whiticar, M. J. (1999). Carbon and hydrogen isotope systematics of bacterial formation and oxidation of methane. *Chemical Geology*, *161*, 291–314. https://doi.org/10.1016/s0009-2541(99)00092-3

Williams, L. B., Hervig, R. L., Wieser, M. E., & Hutcheon, I. (2001). The influence of organic matter on the boron isotope geochemistry of the gulf coast sedimentary basin, USA. *Chemical Geology*, *174*, 445–461. https://doi.org/10.1016/s0009-2541(00)00289-8

Yamashita, Y., Scinto, L. J., Maie, N., & Jaffe, R. (2010). Dissolved organic matter characteristics across a subtropical wetland's landscape: Application of optical properties in the assessment of environmental dynamics. *Ecosystems*, *13*, 1006–1019. https://doi.org/10.1007/s10021-010-9370-1

Yang, J.-W., Ahn, J., Brook, E. J., & Ryu, Y. (2017). Atmospheric methane control mechanisms during the early Holocene. *Climate of the Past*, *13*, 1227–1242. https://doi.org/10.5194/cp-13-1227-2017

Young, N. L., Lemieux, J. M., Delottier, H., Fortier, R., & Fortier, P. (2020). A conceptual model for anticipating the impact of landscape evolution on groundwater recharge in degrading permafrost environments. *Geophysical Research Letters*, *47*, e2020GL087695. https://doi.org/10.1029/2020GL087695